Acta Crystallographica Section D
Biological Crystallography
ISSN 1399-0047

Structure, mechanism and ensemble formation of the alkylhydroperoxide reductase subunits AhpC and AhpF from *Escherichia coli*

Phat Vinh Dip,[a]‡ Neelagandan Kamariah,[b]‡ Malathy Sony Subramanian Manimekalai,[a] Wilson Nartey,[a] Asha Manikkoth Balakrishna,[a] Frank Eisenhaber,[b,c,d] Birgit Eisenhaber[b] and Gerhard Grüber[a,b]*

[a]School of Biological Sciences, Nanyang Technological University, 60 Nanyang Drive, Singapore 637551, Singapore, [b]Bioinformatics Institute, Agency for Science, Technology and Research (A*STAR), 30 Biopolis Street, #07-01 Matrix, Singapore 138671, Singapore, [c]School of Computer Engineering, Nanyang Technological University, 50 Nanyang Drive, Singapore 637553, Singapore, and [d]Department of Biological Sciences, National University of Singapore, 8 Medical Drive, Singapore 117597, Singapore

‡ These authors contributed equally to this work.

Correspondence e-mail: ggrueber@ntu.edu.sg

Received 8 April 2014
Accepted 26 August 2014

PDB references: AhpF, 4o5q; 4o5u; AhpC, 4o5r

Hydroperoxides are reactive oxygen species (ROS) that are toxic to all cells and must be converted into the corresponding alcohols to alleviate oxidative stress. In *Escherichia coli*, the enzyme primarily responsible for this reaction is alkylhydroperoxide reductase (AhpR). Here, the crystal structures of both of the subunits of *Ec*AhpR, *Ec*AhpF (57 kDa) and *Ec*AhpC (21 kDa), have been solved. The *Ec*AhpF structures (2.0 and 2.65 Å resolution) reveal an open and elongated conformation, while that of *Ec*AhpC (3.3 Å resolution) forms a decameric ring. Solution X-ray scattering analysis of *Ec*AhpF unravels the flexibility of its N-terminal domain, and its binding to *Ec*AhpC was demonstrated by isothermal titration calorimetry. These studies suggest a novel overall mechanistic model of AhpR as a hydroperoxide scavenger, in which the dimeric, extended AhpF prefers complex formation with the AhpC ring to accelerate the catalytic activity and thus to increase the chance of rescuing the cell from ROS.

1. Introduction

Redox homeostasis is significant for the survival of the cell and is crucial for defence against reactive oxygen species (ROS) such as hydroperoxides during oxidative stress. ROS, in particular superoxide and hydrogen peroxide, arise from incomplete reduction of oxygen in the respiratory chain, the auto-oxidation of flavoenzymes or exogenous factors such as light, UV radiation and redox-cycling drugs. They are potential sources of damage to various types of macromolecules, leading to protein oxidation, lipid peroxidation and DNA damage (Ames, 1983; Fridovich, 1978; Gutteridge & Halliwell, 1989; Sies, 1993). To prevent such permanent damage, cells have evolved specific defence mechanisms to maintain endogenous ROS at low levels. Peroxiredoxins (prx), which are the primary hydroperoxide scavengers in the cell and reduce hydroperoxides to water and the corresponding alcohol, are widely abundant and highly expressed in organisms from all kingdoms (Seaver & Imlay, 2001; Winterbourn & Hampton, 2008). The members of this family are evolutionarily conserved and are primarily found in the cytosol, although they are also abundant within the mitochondria, chloroplasts and peroxisomes associated with nuclei and membranes (Hofmann *et al.*, 2002). Prx recognizes peroxides and enhances the peroxidative turnover rate with its two redox-active cysteines (Poole & Ellis, 1996). However, a fast catalytic rate, which is essential to rescue the cell from ROS, can only be generated by the well coordinated interaction of prx with peroxiredoxin reductases (prxRs). PrxRs catalyze hydride transfer from NAD(P)H *via* flavin and two different redox-active disulfide bridges to the dithiol centre of prx (Reynolds & Poole, 2000). The interplay between prx and prxR so far

remains uncertain. Understanding this mechanism is a fundamental goal in understanding oxidative stress, which is deeply involved in a number of diseases, such as rheumatoid arthritis, inflammatory bowel disorders and atherosclerosis, and is emerging as one of the most important causative factors of mutagenesis, tumorigenesis and aging (Ames, 1983; Amstad *et al.*, 1990; Cerutti, 1985; Farr & Kogoma, 1991; Floyd, 1990).

Here, we have used biochemical and structural methods to address this issue in order to arrive at a model that explains the role of prx and prxR under oxidative and acidic stress conditions within the cell. The *Escherichia coli* system, involving its alkyl hydroperoxide reductase (AhpR) enzyme consisting of the 57 kDa subunit AhpF (prxR) and the 21 kDa AhpC (prx) proteins, which are among the ten most abundant *E. coli* proteins (Link *et al.*, 1997), is an ideal candidate to obtain a profound and detailed model. The reduction of peroxides occurs *via* the redox-active centre of AhpC in the reduced state which becomes restored by AhpF, which transfers electrons from NADH to AhpC. The catalytic mechanism of AhpF has been proposed to follow a path similar to that of thioredoxin reductase (TrxR), which is an important intracellular reduction system (Tartaglia *et al.*, 1990; Reynolds & Poole, 2000). AhpF consists of three domains: an N-terminal domain (NTD), an FAD-binding domain and an NADH-binding domain. The structures of the crystallographic homodimer of the C-terminal region of *E. coli* AhpF (*Ec*AhpF$_{212–521}$; Bieger & Essen, 2001) as well as of full-length AhpF from *Salmonella typhimurium* (*St*AhpF; PDB entry 1hyu; Wood *et al.*, 2001) reveal the FAD and NADH domains. The C-terminal regions of both structures show a high similarity to the atomic structures of the related *E. coli* thioredoxin reductase (TrxR; Kuriyan *et al.*, 1991; Lennon *et al.*, 2000; Waksman *et al.*, 1994), which demonstrated that the NADH-binding domain of AhpF is required to alternate between at least two structural states known as the flavin-reduced state (FR) and the flavin-oxidized state (FO) in order to carry out the series of intramolecular electron transfers between the redox centres for catalysis (Bieger & Essen, 2001; Kuriyan *et al.*, 1991; Lennon *et al.*, 2000; Waksman *et al.*, 1994).

To date, no structural details of *Ec*AhpC have been described. It has been proposed to undergo an oligomerization equilibrium between a dimer and a decamer (Wood *et al.*, 2002). Despite many studies, the mechanism of the dithiol–disulfide exchange from AhpF to AhpC, in particular the critical conformations of AhpF and its catalytically relevant intermediate forms during catalysis, is still poorly understood. The importance of AhpC oligomer formation is still not clear, and hence investigation into its dimeric or high-molecular-weight (HMW) complex form is therefore of great interest. The data presented here provide the first full-length crystal structure of *E. coli* AhpF at 2.65 and 2.0 Å resolution. The structures reveal for the first time an alternative conformation of the N-terminal domain which is identified to be the AhpF–AhpC binding epitope that transfers electrons from AhpF to its substrate AhpC. The conformation of *Ec*AhpF was validated in solution using small-angle X-ray scattering (SAXS). The crystal structure of the decameric *Ec*AhpC in an oxidized form was solved at 3.3 Å resolution. The novel open conformation of the dimeric AhpF (prxR) presented here favours binding of AhpC (prx) in its decameric ring structure during catalytic activity to assure the rapid reduction of hydrogen peroxide. This detailed model will open up future research opportunities to tackle ROS detoxification and its relevance to senescence, aging and disease.

2. Experimental procedures

2.1. Protein purification of *E. coli* AhpF

E. coli cells were lysed on ice in buffer *A* (50 m*M* Tris–HCl pH 8, 500 m*M* NaCl, 2 m*M* PMSF, 1 m*M* Pefabloc SC, 0.8 m*M* DTT) by sonication with an ultrasonic homogenizer (Bandelin, KE76 tip) for 3 × 1 min. After sonication, the cell lysate was centrifuged at 10 000*g* for 35 min at 277 K. The resulting supernatant was passed through a filter (0.45 mm pore size) and supplemented with Ni–NTA resin pre-equilibrated in buffer *A*. The protein was allowed to bind to the matrix for 2 h at 277 K by mixing on a sample rotator (Neolab) and was eluted with an imidazole gradient (0–100 m*M*) in buffer *A*. Fractions containing *Ec*AhpF were identified by SDS–PAGE (Laemmli, 1970), applied onto a Resource Q (6 ml; GE Healthcare) column and eluted with an NaCl gradient. The collected *Ec*AhpF was concentrated and subsequently purified by size-exclusion chromatography (Superdex HR75, GE Healthcare). The purity of the protein sample was analyzed by SDS–PAGE (Laemmli, 1970) stained with Coomassie Brilliant Blue R250.

2.2. Crystallization of *Ec*AhpF

The purified protein was concentrated to 10 mg ml^{-1} in 50 m*M* Tris–HCl pH 8, 230 m*M* NaCl using a 10 kDa cutoff concentrator. Preliminary screening for initial crystallization conditions was performed by the hanging-drop vapour-diffusion method using screens from Hampton Research at 296 K. 1 µl concentrated protein solution was mixed with an equal volume of reservoir solution and was equilibrated over 500 ml reservoir solution using 24-well Cryschem plates (Hampton Research). In the initial screening, small needle-shaped crystals were obtained after several days in condition 4 (0.1 *M* Tris pH 8.5, 2.0 *M* ammonium sulfate) and condition 39 [0.1 *M* Na HEPES pH 7.5, 2%(*v*/*v*) PEG 400, 2 *M* ammonium sulfate] from Crystal Screen at 293 K. Both conditions were optimized by varying the protein, precipitant and salt concentrations, the pH and the temperature, and by the use of an additive screen. Cadmium chloride hydrate was identified as an additive that produced a cluster of needles. Micro-seeding with the needle crystals obtained in condition 4 using a seed bead (Hampton Research) yielded plate-shaped single crystals with good diffraction quality. Finally, optimized native crystals with dimensions of 0.2 × 0.1 × 0.03 mm were grown under this condition using protein at 3 mg ml^{-1} concentration in 0.1 *M* Tris–HCl pH 8.5, 2 *M* ammonium sulfate, 10 m*M* cadmium chloride. Condition 39 was further optimized and suitable crystals for X-ray diffraction measurements with

Table 1
Data-collection, processing and refinement statistics for the *E. coli* AhpF and AhpC structures.

Values in parentheses are for the highest resolution shell. Values in square brackets are anomalous statistics.

	AhpF					
		Dy derivative				
	Native 1	Peak	Inflection	High-energy remote	Native 2	AhpC
Wavelength (Å)	1.000	1.58994	1.59048	1.55072	1.000	1.000
Crystal-to-detector distance (mm)	380	250	250	250	280	500
Rotation range per image (°)	1	1	1	1	1	0.2
Total rotation range (°)	200	360	180	180	360	100
Exposure time per image (s)	15	5	5	5	10	0.2
Space group	*C*2	*C*2	*C*2	*C*2	*C*2	$P3_121$
Unit-cell parameters						
a (Å)	106.70	106.83	106.66	106.89	106.49	137.35
b (Å)	59.60	59.49	59.41	59.49	58.70	137.35
c (Å)	123.71	124.37	123.79	124.10	123.99	147.45
α (°)	90	90	90	90	90	90
β (°)	113.68	114.16	114.19	114.20	114.58	90
γ (°)	90	90	90	90	90	120
Molecules in asymmetric unit	1	1	1	1	1	5
Solvent content (%)	61.7	61.7	61.4	61.6	59.1	68.2
Resolution limits (Å)	30.0–2.65 (2.74–2.65)	50.0–3.40 (3.52–3.40)	50.0–3.05 (3.16–3.05)	50.0–3.05 (3.16–3.05)	30.0–2.00 (2.07–2.00)	30.0–3.33 (3.51–3.33)
No. of reflections	82259	57749	45865	45375	346921	78071
Unique reflections	21022	10341	13808	13793	45054	23735
Multiplicity	4 (3.2)	6.0 (3.6) [3.1]	3.4 (2.4) [1.8]	3.4 (2.3) [1.8]	7.3 (6.3)	3.3 (3.1)
Completeness (%)	99.0 (92.8)	95.0 (74.5) [94.1]	97.0 (79.9) [94.1]	96.8 (78.8) [93.7]	99.7 (98.6)	99.2 (99.7)
$R_{\rm merge}$† (%)	9.8 (34.1)	15.9 (35.6) [13.4]	9.7 (32.0) [7.6]	9.6 (34.8) [7.9]	6.7 (49.6)	6.7 (48.4)
$\langle I/\sigma(I)\rangle$	12.9 (3.2)	6.5 (1.6) [4.9]	7.7 (1.3) [5.7]	7.4 (1.2) [5.5]	20.4 (2.1)	10.2 (2.5)
Refinement statistics						
R factor‡ (%)	17.18 (24.46)				14.14 (17.88)	24.07 (33.19)
$R_{\rm free}$§ (%)	22.04 (29.05)				18.78 (22.40)	25.33 (33.77)
No. of waters	162				503	
No. of sulfates	8				8	
No. of FAD molecules	1				1	
No. of cadmium ions	1				1	
No. of PEG molecules					7	
No. of glycerol molecules					7	
No. of Tris molecules					1	
MolProbity statistics						
Ramachandran favoured (%)	95.38				97.93	98.18
Ramachandran outliers (%)	0				0.19	0.12
Clashscore	1.24				3.29	0.47
R.m.s. deviations						
Bond lengths (Å)	0.006				0.012	0.004
Bond angles (°)	0.91				1.41	0.70
Overall *B* values (Å^2)						
From Wilson plot (Å^2)	43.3	45.6	64.5	63.9	40.2	
Mean *B* value (Å^2)	44.7				40.8	62.3

† $R_{\rm merge} = \sum_{hkl}\sum_i |I_i(hkl) - \langle I(hkl)\rangle| / \sum_{hkl}\sum_i I_i(hkl)$, where $\langle I(hkl)\rangle$ is the mean intensity for reflection *hkl*. ‡ *R* factor $= \sum_{hkl} \big||F_{\rm obs}| - |F_{\rm calc}|\big| / \sum_{hkl} |F_{\rm obs}|$, where $F_{\rm obs}$ and $F_{\rm calc}$ are measured and calculated structure factors, respectively. § $R_{\rm free} = \sum_{hkl} \big||F_{\rm obs}| - |F_{\rm calc}|\big| / \sum_{hkl} |F_{\rm obs}|$ calculated from 5% of the reflections that were selected randomly and omitted during refinement.

dimensions of 0.3 × 0.12 × 0.05 mm were obtained by the sitting-drop vapour-diffusion method at 25°C using protein at 2 mg ml^{-1} concentration and a solution consisting of 0.1 *M* Na HEPES pH 7.5, 2.5%(*v*/*v*) PEG 400, 2 *M* ammonium sulfate, 10 m*M* cadmium chloride. Diffraction-quality crystals obtained under these different conditions were soaked in a cryoprotectant solution comprising their respective reservoir solutions supplemented with 20% glycerol and were flash-cooled in liquid nitrogen for data collection.

Heavy-atom derivatives were prepared by soaking native crystals of the *E. coli* AhpF protein in crystallization buffer supplemented with heavy-atom solution. The crystals were only stable in the presence of samarium and dysprosium derivatives. For the samarium-derivatized crystals no useful anomalous signal could be observed. Dysprosium-derivative crystals were obtained by soaking a single crystal in crystallization solution supplemented with 20% glycerol and 10 m*M* dysprosium(III) chloride for 4 h.

2.3. Data collection and structure determination of *Ec*AhpF

A single-wavelength data set for the native *E. coli* AhpF protein and a three-wavelength multiwavelength anomalous diffraction (MAD) data set for the dysprosium derivative were collected at 140 K on beamline 13B1 at the National Synchrotron Radiation Research Center (NSRRC), Hsinchu,

Taiwan using an ADSC Quantum 315 CCD detector. A complete 3.1 Å resolution MAD data set was collected based on the dysprosium absorption spectrum at the appropriate inflection, peak and high-remote wavelengths using a single crystal. The native data sets for *Ec*AhpF were collected to 2.65 and 2.0 Å resolution from single crystals grown under the optimized conditions 4 and 39, respectively. All diffraction data were indexed, integrated and scaled using the *HKL*-2000 suite of programs (Otwinowski & Minor, 1997). The results of data processing and the data statistics are summarized in Table 1.

Initially, the phases for the *Ec*AhpF molecule were determined at 3.1 Å resolution by the three-wavelength MAD technique using the dysprosium heavy-atom derivative with *autoSHARP* (Vonrhein *et al.*, 2007). Two sites for the Dy atom could be identified: a major site with 100% occupancy and a minor site with 46% occupancy. Density modification with 60% solvent content yielded continuous density with distinct secondary-structural features. The initial phases obtained were solvent-flattened using *SOLOMON* (Abrahams & Leslie, 1996) and were combined with the 2.65 Å resolution native data set. An initial atomic model was built using *AutoBuild* in *PHENIX* (Adams *et al.*, 2009). A more complete model was built using *ARP*/*wARP* (Langer *et al.*, 2013). Iterative cycles of manual model building and refinement were carried out using *Coot* (Emsley & Cowtan, 2004) and *REFMAC*5 (Murshudov *et al.*, 2011) from the *CCP*4 suite (Winn *et al.*, 2011) to build the final model. Refinement with *phenix.refine* (Afonine *et al.*, 2012) was performed until convergence, and the geometry of the final model was validated with *MolProbity* (Chen *et al.*, 2010; Table 1). The native *Ec*AhpF structure was solved by the molecular-replacement method with the high-resolution native data set using the *S. typhimurium* AhpF structure (PBD entry 1hyu; Wood *et al.*, 2001) as the model in *Phaser* (McCoy *et al.*, 2007). The starting model was improved manually using *Coot* between iterative cycles of restrained refinement by *REFMAC*5 from the *CCP*4 suite to improve the phases. Refinement with *phenix.refine* was performed until convergence, and the geometry of the final model was validated with *MolProbity*. The figures were drawn using *PyMOL* (DeLano, 2002) and structural comparison analysis was carried out using *SUPERPOSE* (Krissinel & Henrick, 2004), as included in the *CCP*4 suite, and *PDBeFold* (Krissinel & Henrick, 2005). The overall conformational changes between the structures were analyzed using *DynDom* (Hayward & Berendsen, 1998). The accessible surface area was calculated by *WHAT IF* (Vriend, 1990) and the interface analysis was carried out by *PDBePISA* (Krissinel & Henrick, 2007). Each *Ec*AhpF monomer contained 521 amino-acid residues with almost all of the main-chain residues fitting well into the electron density (Supplementary Fig. S1*b*[1]), except for residues Thr197–Glu200 and Gly198–Lys201 in the 2.65 and 2.0 Å resolution structures, respectively. Beside the FAD molecule, one cadmium ion and eight sulfate ions were observed in both of the structures. The 2.0 Å resolution structure also contains a few PEG and glycerol molecules and a Tris molecule (Table 1). The coordinates and structure factors of the native *Ec*AhpF at 2.65 and 2.0 Å resolution have been deposited in the PDB with accession codes 4o5u and 4o5q, respectively.

2.4. Cloning, overexpression and purification of AhpF-NTD and AhpF-CTD

The coding regions for the N-terminal domain (AhpF-NTD; residues 1–196) and C-terminal domain (AhpF-CTD; residues 212–521) of *Ec*AhpF were amplified by polymerase chain reaction using the forward primer 5′-CATT**CCATGG**CAATGCTCGACACAAATATG-3′ and the reverse primer 5′-GT**C**GAGCTC**C**TTAATCAATTTTGGCAACGAT-3′ for AhpF-NTD and the forward primer 5′-CATG**CCATGG**CTTATGACGTATTAATCGTC-3′ and the reverse primer 5′-GC**GAGCTC**GTTATGCAGTTTTGGTGCGAAT-3′ for AhpF-CTD. In all cases, the restriction sites (bold) for the *Nco*I and *Sac*I enzymes were used in the forward and reverse primers, respectively. The amplified products were ligated into the pET9-d1-His_6 vector (Grüber *et al.*, 2002). The respective coding sequences were verified by DNA sequencing. The final plasmids were subsequently transformed into *E. coli* BL21 (DE3) cells (Stratagene). To express the individual proteins, liquid cultures were shaken in LB medium containing kanamycin (30 µg ml^{-1}) for about 6 h at 310 K until an optical density OD_{600} of 0.6–0.7 was reached. To induce the production of proteins, cultures were supplemented with isopropyl β-D-1-thiogalactopyranoside (IPTG) to a final concentration of 1 m*M* followed by incubation for 4 h at 310 K.

Cells producing the AhpF-NTD or AhpF-CTD protein were lysed on ice by sonication with an ultrasonic homogenizer (Bandelin, KE76 tip) for 3 × 1 min in buffer *A* (50 m*M* Tris–HCl pH 7.5, 200 m*M* NaCl, 2 m*M* PMSF, 1 m*M* Pefabloc SC, 0.8 m*M* DTT). After sonication, the cell lysate was centrifuged at 10 000*g* for 35 min at 277 K. The resulting supernatant was passed through a filter (0.45 µm; Millipore) and supplemented with Ni^{2+}–NTA resin pre-equilibrated in the respective buffer. The His-tagged proteins were allowed to bind to the matrix for 1.5 h at 277 K by mixing on a sample rotator (Neolab). To avoid any traces of residual DTT from the lysis buffer, the Ni^{2+}–NTA resin was thoroughly washed with ten column volumes of the respective buffer without DTT and was subsequently eluted with an imidazole gradient (0–500 m*M*). Subsequently, the fractions containing AhpF-NTD or AhpF-CTD were identified by SDS–PAGE (Laemmli, 1970) and applied onto a Resource Q column (6 ml; GE Healthcare). AhpF-NTD eluted in the flowthrough, whereas AhpF-CTD was eluted with an NaCl gradient. The flowthrough of the AhpF-NTD and respective fractions containing AhpF-CTD were concentrated and further purified by gel-filtration chromatography using a Superdex 75 HR 10/30 column (GE Healthcare) with buffer consisting of 50 m*M* Tris–HCl pH 7.5, 200 m*M* NaCl.

[1] Supporting information has been deposited in the IUCr electronic archive (Reference: BE5266).

2.5. Cloning, production and purification of *Ec*AhpC

The coding region for the entire *E. coli* AhpC (SWISS-PROT accession No. P0AE08) was amplified by PCR using the forward primer 5′-CATG**CCATGG**CAATGTCCTTGATTA-ACACC-3′ with an *Nco*I restriction site (bold) and the reverse primer 5′-GC**GAGCTC**GTTAGATTTTACCAACCAGGTC-3′ with an *Sac*I restriction site (bold), respectively. The amplified products were ligated into the pET9-d1-His_6 vector (Grüber *et al.*, 2002). The AhpC coding sequences were verified by DNA sequencing. The final plasmid was subsequently transformed into *E. coli* BL21 (DE3) cells (Stratagene). To induce the production of proteins, the cultures were supplemented with IPTG to a final concentration of 1 m*M* followed by incubation for 4 h at 310 K. Recombinant *E. coli* AhpC was purified according to the protocol described above for AhpF-CTD.

2.6. Crystallization of oxidized *Ec*AhpC

The purified oxidized form of full-length AhpC was concentrated to 8 mg ml^{-1} in buffer consisting of 50 m*M* Tris–HCl pH 7.5, 200 m*M* NaCl using a 10 kDa cutoff concentrator. Initial crystallization screening was carried out by the hanging-drop vapour-diffusion method at 291 K using Crystal Screen and Crystal Screen 2 from Hampton Research (Jancarik & Kim, 1991) and Wizard I and II (Emerald Bio) in 48-well VDX plates (Hampton Research). Initially slight precipitation was observed, followed by small crystals appearing 14 d later in Crystal Screen 2 [1.8 *M* ammonium sulfate, 100 m*M* 2-(*N*-morpholino)ethanesulfonic acid pH 6.5, 10% dioxane]. Crystals were optimized by systematically performing a grid screen by varying the concentrations of precipitant and salt, the buffer pH and the protein concentration. The best crystals appeared in 1.8 *M* ammonium sulfate, 100 m*M* MES pH 6.5, 5% dioxane with a protein concentration of 8 mg ml^{-1}.

2.7. Data collection and structure determination of *Ec*AhpC

The crystal was quick-soaked in a cryoprotectant solution containing 25% glycerol in mother liquor and flash-cooled in liquid nitrogen at 100 K. A single-wavelength data set for AhpC was collected on the S06 PX protein crystallography beamline at the Swiss Light Source (SLS) using a PILATUS 6M detector. Data were collected as a series of 0.2° oscillation images with 0.2 s exposure time and a crystal-to-detector distance of 500 mm. All diffraction data were indexed, integrated and scaled using *iMosflm* (Battye *et al.*, 2011). The results of data processing and data statistics for *Ec*AhpC are summarized in Table 1. The structure of *Ec*AhpC was solved by the molecular-replacement method using the *S. typhimurium* AhpC structure (PBD entry 3emp; Nelson *et al.*, 2008) as a model with *Phaser* (McCoy *et al.*, 2007). To improve the electron density by solvent flattening and to reduce the model bias, prime-and-switch phasing was performed using *RESOLVE* (Terwilliger, 2004). Subsequent rigid-body and restrained refinement was performed with *REFMAC*5 and the starting model was improved manually using *Coot* (Emsley & Cowtan, 2004). Refinement was performed until convergence, and the geometry of the final model was validated with *MolProbity* (Chen *et al.*, 2010). Structural comparison analysis was carried out using *SUPERPOSE* (Krissinel & Henrick, 2004) as included in the *CCP*4 suite. The crystal structure of *Ec*AhpC contains five molecules (*A*–*E*) in the asymmetric unit and has clear electron density for all main-chain atoms except for the C-terminal region, which is highly disordered (Supplementary Fig. S4). Only two disulfide bonds (*A* Cys166–*B* Cys47 and *C* Cys166–*D* Cys47) were observed among the five *Ec*AhpC molecules. This may be owing to the highly disordered C-terminus and may also possibly be owing to radiation damage. The coordinates and structure factors of *Ec*AhpC have been deposited in the PDB with accession code 4o5r.

2.8. Solution small-angle X-ray scattering of *Ec*AhpF

Small-angle X-ray scattering (SAXS) data for *Ec*AhpF were measured using a NANOSTAR instrument (Bruker) equipped with a metal-jet X-ray source and a Vantec 2000 detector system. The metal-jet source uses a liquid gallium source to deliver a high-intensity X-ray beam at a wavelength of 1.34 Å. SAXS measurements were carried out with a two-pinhole collimation system and a sample-to-detector distance of 67 cm. Protein concentrations of 1.0, 2.2, 4.1, 5.8 and 8.5 mg ml^{-1} *Ec*AhpF were measured at 15°C (sample volume of 40 µl). The buffer consisted of 50 m*M* Tris pH 7.5, 200 m*M* NaCl. For each concentration, a total of six measurements were recorded at 5 min intervals. The data were flood-field and spatially corrected and processed using the in-built SAXS software. The data were tested for possible radiation damage by comparing the six data sets and no changes were detected. The scattering of the buffer was subtracted and the difference curves were scaled for concentration. All data-processing steps were performed automatically using the *PRIMUS* program package (Svergun, 1993). The forward scattering $I(0)$ and the radius of gyration R_g were evaluated using the Guinier approximation (Guinier & Fournet, 1955). These parameters were also computed from the entire scattering patterns using the indirect transform package *GNOM* (Svergun, 1992), which also provided the distance distribution function $p(r)$. Low-resolution models of *Ec*AhpF were built by *GASBOR* (Svergun *et al.*, 2001). *Ab initio* solution shapes of *Ec*AhpF were obtained by the superposition of ten independent model reconstructions with the *SUPCOMB* program package (Kozin & Svergun, 2001) and building an averaged model from the most probable model using *DAMAVER* (Volkov & Svergun, 2003). Comparison of experimental scattering curve with the theoretical scattering curves calculated for the monomer and the dimer of *St*AhpF (PDB entry 1hyu) and *Ec*AhpF were performed with *CRYSOL* (Svergun *et al.*, 1995). The curves were then used in *OLIGOMER* (Konarev *et al.*, 2003) to find the best fit to a multi-component mixture of proteins.

SAXS data sets for AhpF-NTD (residues 1–196) and AhpF-CTD (residues 212–521) were collected at protein concentrations of 8.5 and 8.45 mg ml^{-1}, respectively, and their solution shapes were determined as described above.

2.9. NADH-dependent peroxidase activity

The NADH-dependent peroxidase assay was monitored at 340 nm by following the decrease in NADH absorbance. The assay was carried out at 25°C in a total volume of 100 µl consisting of 300 µ*M* NADH, 1 m*M* hydrogen peroxide, 1 µ*M* both AhpF and AhpC and 50 m*M* phosphate buffer pH 7.0 containing 100 m*M* ammonium sulfate and 0.5 m*M* EDTA. All of the reaction-mixture components were added to the reaction buffer except for the NADH, which was added at the end to start the reaction. The background reaction measured for all mixtures without AhpC was taken as a control. The maximum NADH oxidation activity observed in the presence

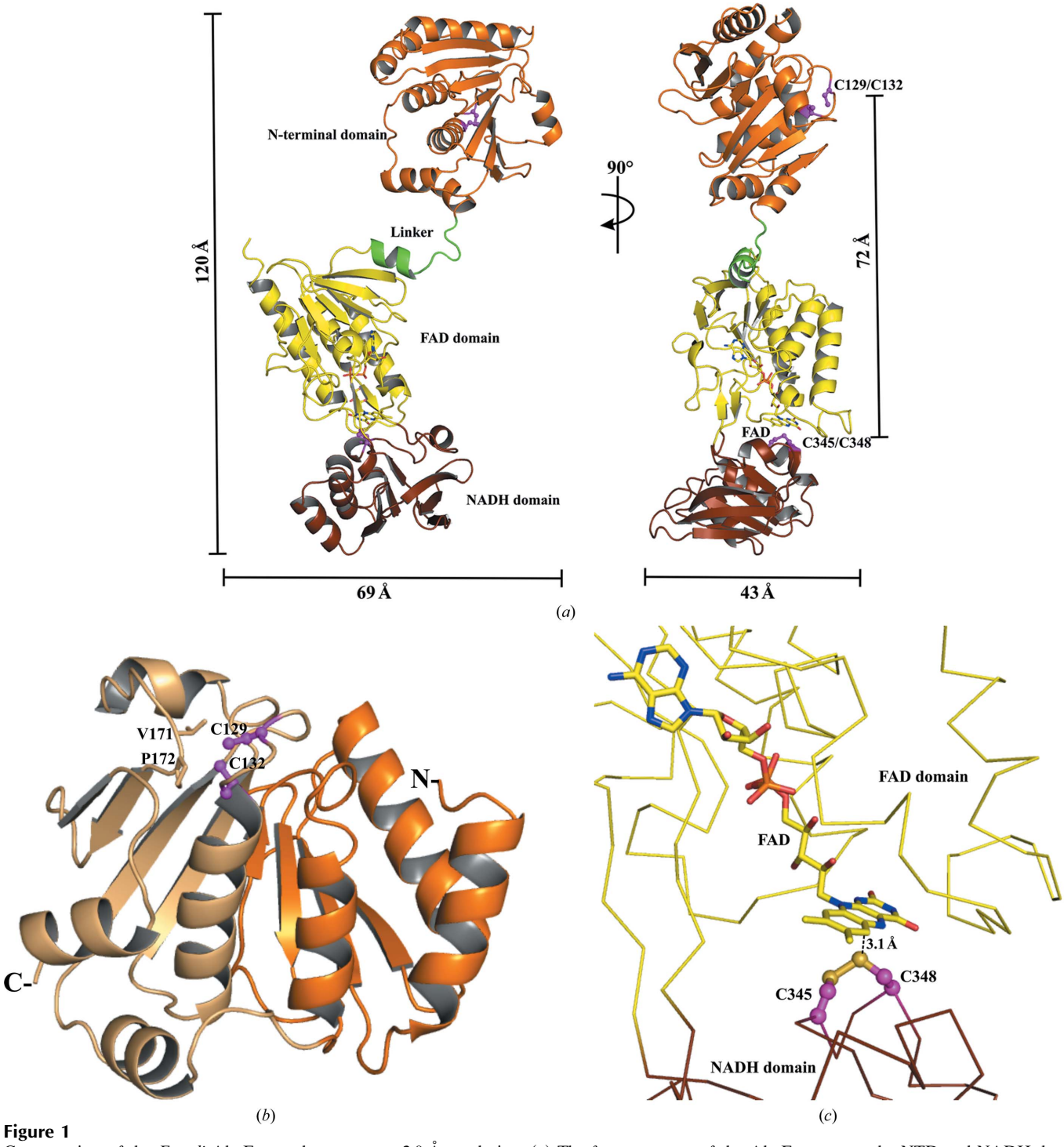

Figure 1
Cartoon view of the *E. coli* AhpF crystal structure at 2.0 Å resolution. (*a*) The four segments of the AhpF structure; the NTD and NADH domain contain the redox-active disulfide centres (magenta). In the 90° rotated view, the flavin cofactor in the FAD domain is clearly shown in the structure. (*b*) The NTD is made up of two Trx-like domains fused together (orange and pale orange). The redox-active centre is found only in the C-terminal half of the Trx-like domain. (*c*) Contacts between the FAD and NADH domains are mainly formed by interactions between the isoalloxazine ring of the FAD cofactor and the NADH-domain redox centre, with a shortest distance of 3.1 Å.

of AhpC was saturated at 6 min. The NADH oxidation was measured with multi-wavelength scanning ranging from 280 to 540 nm on two different time scales. The first measurement was carried out immediately after the reaction mixture had been added and the second measurement was performed after 6 min, when the NADH oxidation was saturated for AhpC.

2.10. Interaction studies of AhpF-NTD and AhpF-CTD with *Ec*AhpC

Isothermal titration calorimetry experiments were carried out with a VP-ITC microcalorimeter (MicroCal, Northampton, England) to study the binding of AhpF-NTD and AhpF-CTD to *E. coli* AhpC. All of the proteins were prepared in a common buffer composed of 50 m*M* Tris–HCl, 200 m*M* NaCl pH 7.5 to minimize the buffer-dilution effect during the experiments. Samples were centrifuged and degassed before the ITC studies. All of the experiments were performed using 755 µ*M* AhpF-NTD and AhpF-CTD titrated against 31 µ*M* AhpC at 293 K. In all cases control experiments were performed with the ligand and the buffer. The dissociation constant was determined by the least-squares method and the binding isotherm was fitted using the in-built *Origin* v.7.0 software (MicroCal) assuming a single-site binding model.

3. Results

3.1. Crystallographic structures of *E. coli* AhpF

The crystal structure of *E. coli* AhpF (57 kDa) has been solved at 2.65 and 2.0 Å resolution. In both structures one molecule was observed in the asymmetric unit (Table 1). The extended *Ec*AhpF molecule has dimensions of 120.5 × 68.9 × 43.2 Å and consists of four regions: the N-terminal domain (NTD; residues 1–196), a linker (residues 197–209), the FAD domain (residues 210–327 and 450–521) and the NADH domain (residues 328–449) (Fig. 1*a*). Overall, three redox centres are present in the structure: the FAD molecule in the FAD domain, the residues Cys345/Cys348 in the NADH domain and the residues Cys129/Cys132 in the NTD. The redox-active disulfide (Cys345/Cys348) is in close proximity to the flavin, but is 72 Å away from Cys129/Cys132 in the NTD (Fig. 1*a*). A dimer of *Ec*AhpF is formed with a symmetry-related molecule generated by the crystallographic twofold axis, revealing a head-to-tail dimerization mode (Supplementary Fig. S1*a*). The homodimer of *Ec*AhpF is elongated, with a distance of 125 Å between the two NTD redox-active disulfide centres Cys129/Cys132 (Supplementary Fig. S1*a*), giving the possibility of electron transfer to the redox-active disulfide bond in AhpC, which will be discussed later.

The 2.65 and 2.0 Å resolution structures are similar, with an r.m.s. difference in C^{α} positions of 0.72 Å for the 521 residues in the monomer. When the FAD domain alone was overlaid,

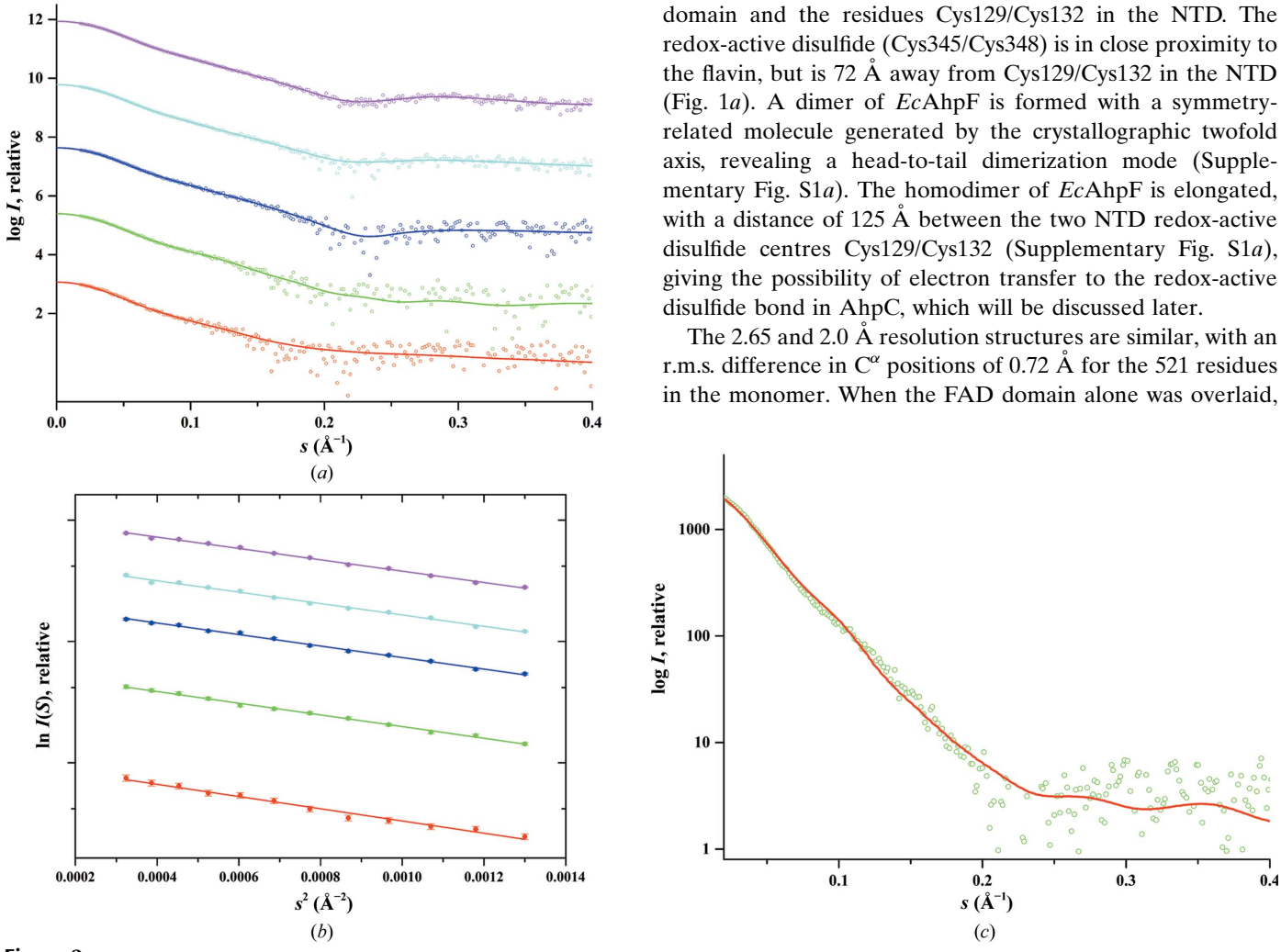

Figure 2
Solution X-ray scattering studies of *Ec*AhpF. (*a*) Small-angle X-ray scattering patterns (circles) and the corresponding experimental fitting curves for concentrations of 1.0 mg ml^{-1} (red), 2.2 mg ml^{-1} (green), 4.1 mg ml^{-1} (blue), 5.8 mg ml^{-1} (cyan) and 8.5 mg ml^{-1} (magenta). The curves for *E. coli* AhpF are displayed in logarithmic units for clarity. (*b*) Guinier plots show linearity for the concentrations used, indicating no aggregation. (*c*) Theoretical scattering curve (red) for the mixture of 53% open and 47% closed dimers of *Ec*AhpF calculated using *OLIGOMER* that fits the experimental scattering pattern (circles) for the 4.1 mg ml^{-1} concentration data with a χ value of 1.53.

the NTD adopts two different conformations, with a rotation of 2.8° around an axis along the molecule (Supplementary Fig. S1*c*). Structurally, the NTD of *Ec*AhpF consists of two 'fused' so-called N- and C-terminal thioredoxin folds (Fig. 1*b*). The NTD redox centre ($_{129}$C*XX*C$_{132}$) is located in the C-terminal thioredoxin fold, which in the 2.0 Å resolution structure is reduced to its dithiol form with a distance of 3.04 Å (Supplementary Fig. S1*b*), although no reducing agent was used during crystallization. As described for the NTD redox centre of *St*AhpF, cleavage of the disulfide bond might be caused by synchrotron-radiation damage (Wood *et al.*, 2001; Roberts *et al.*, 2005). In comparison to Cys132, the Cys129 residue is exposed to the surface, while the hydrophobic amino acids Val171 and *cis*-Pro172 cover Cys132 and make it solvent-inaccessible. In comparison, Cys129 and Cys132 form a disulfide bond with an S—S distance of 2.05 Å in the 2.65 Å resolution structure (Supplementary Fig. S1*b*). The change in the χ angle for Cys129 (which changes from −173° to −175°) and for Cys132 (from −49° to −83°) between the disulfide and dithiol forms could be the result of disulfide breakage. Subtle differences in torsion angles are also observed in the vicinity of the redox centre in the region from Leu127 to Pro133. Furthermore, few polar and nonpolar interactions are observed in the reduced form, which might stabilize the cysteines. Interestingly, a six-coordinate cadmium ion was found to be adjacent to the redox centre of the NTD (Supplementary Fig. S1*d*). The linker region of *Ec*AhpF, which adopts a loop–helix conformation, connects the NTD to the FAD domain (Supplementary Fig. S1*c*).

The FAD and NADH domains of *Ec*AhpF have similar structural features consisting of a β-sandwich formed by a five-stranded parallel β-sheet on one side and a three-stranded antiparallel β-sheet on the other side, which is flanked by three α-helices and a short helix on the other side (Fig. 1*a*). The cofactor FAD is present in both structures and is accommodated well in the binding pocket of the FAD domain (Fig. 1*c*). In both *Ec*AhpF structures a sulfate ion and glycerol and PEG molecules have been observed in the NADH-binding channel (Supplementary Fig. S2). The NADH domain is responsible for NADH binding and contains the C-terminal redox centre $_{345}$C*XX*C$_{348}$, which is in close vicinity to the FAD cofactor (Fig. 1*c*), adopting a short helix with a right-handed hooked disulfide conformation. The NADH domain is connected to the FAD domain through two short polypeptide stretches Leu325–Asn327 and Gln448–Leu451. When compared with the NTD, the FAD and NADH domains have low temperature factors.

3.2. *Ec*AhpF in solution studied by SAXS

Small-angle X-ray scattering (SAXS) experiments were performed in order to study the overall conformation of *Ec*AhpF in solution. SAXS patterns of *Ec*AhpF were recorded at different concentrations (see Table 2) to yield the final composite scattering curves as shown in Fig. 2(*a*). The Guinier plots at low angles are linear and revealed good data quality with no indication of protein aggregation (Fig. 2*b*). The radius of gyration (R_g) values from the Guinier approximation were consistent for all of the concentrations measured (ranging from 37.7 to 39.5 Å; Table 2). The distribution functions, $p(r)$, determined were similarly shaped for all of the concentrations used (Supplementary Fig. S3*b*). The maximum particle dimensions (D_{max}; 131–138 Å) point to an elongated shape that displays an asymmetrical tail, as is typical for elongated particles. The gross shape of the *Ec*AhpF was reconstructed *ab initio* and had a good fit to the experimental data in the entire scattering range and had a discrepancy of χ^2 = 0.986 (Supplementary Fig. S3*a*). The average structure of ten independent reconstructions is shown in Supplementary Fig. S3(*c*).

Table 2
SAXS statistics for the different concentrations of *Ec*AhpF measured.

AhpF concentration (mg ml^{-1})	R_g† (Å)	R_g‡ (Å)	D_{max} (Å)
1.0	39.5 ± 1.02	42.10 ± 0.43	138.2
2.2	38.2 ± 0.55	40.40 ± 0.34	135.5
4.1	38.0 ± 0.37	39.81 ± 0.20	134.2
5.8	37.6 ± 0.29	39.27 ± 0.14	130.3
8.5	37.7 ± 0.23	39.09 ± 0.15	131.2

† Determined by Guinier approximation. ‡ Determined by *GNOM*.

Since the present *Ec*AhpF crystal structures, like that of *S. typhimurium* AhpF (Wood *et al.*, 2001), have been shown to contain dimers, the theoretical scattering curves of the extended monomeric and dimeric *Ec*AhpF crystal structure as well as the closed monomer and dimer of *St*AhpF (PDB entry 1hyu) were computed using *CRYSOL* (Svergun *et al.*, 1995). When compared with the experimental solution X-ray scattering data of *Ec*AhpF, the scattering pattern computed from the crystallographic model of the dimeric form of the extended *Ec*AhpF (χ = 2.1) and closed *St*AhpF (χ = 2.2) conformations had a better fit than the monomeric extended *Ec*AhpF (χ = 4.4) or closed *St*AhpF (χ = 5.1) conformations (Supplementary Fig. S3*d*). Based on the good χ values of the dimeric forms, the percentage of open and closed conformation was calculated using *OLIGOMER* (Konarev *et al.*, 2003). A good fit with a χ value of 1.5 was obtained when both conformations were similarly populated, with that of the extended open dimer being slightly higher (53%; Fig. 2*c*). Taken together, at all of the concentrations measured AhpF exists as a dimer in solution with an equal mixture of both extended open and closed conformations as determined by *OLIGOMER*.

3.3. Crystal structure of *E. coli* AhpC

Besides AhpF, the *E. coli* AhpR system consists of the 21 kDa AhpC subunit, which reduces peroxides *via* its redox-active disulfide centre, while AhpF restores the reduced state of AhpC by transferring electrons from NADH to AhpC. The 187-amino-acid AhpC from *E. coli* has been produced and purified and its NADH-dependent peroxidative activity has been monitored at 340 nm by following the decrease in NADH absorbance (Fig. 3*a*). All of the reaction-mixture components were added to the reaction buffer except for the NADH, which was added at the end to start the reaction. The peroxidase assay was performed with *Ec*AhpF and *Ec*AhpF

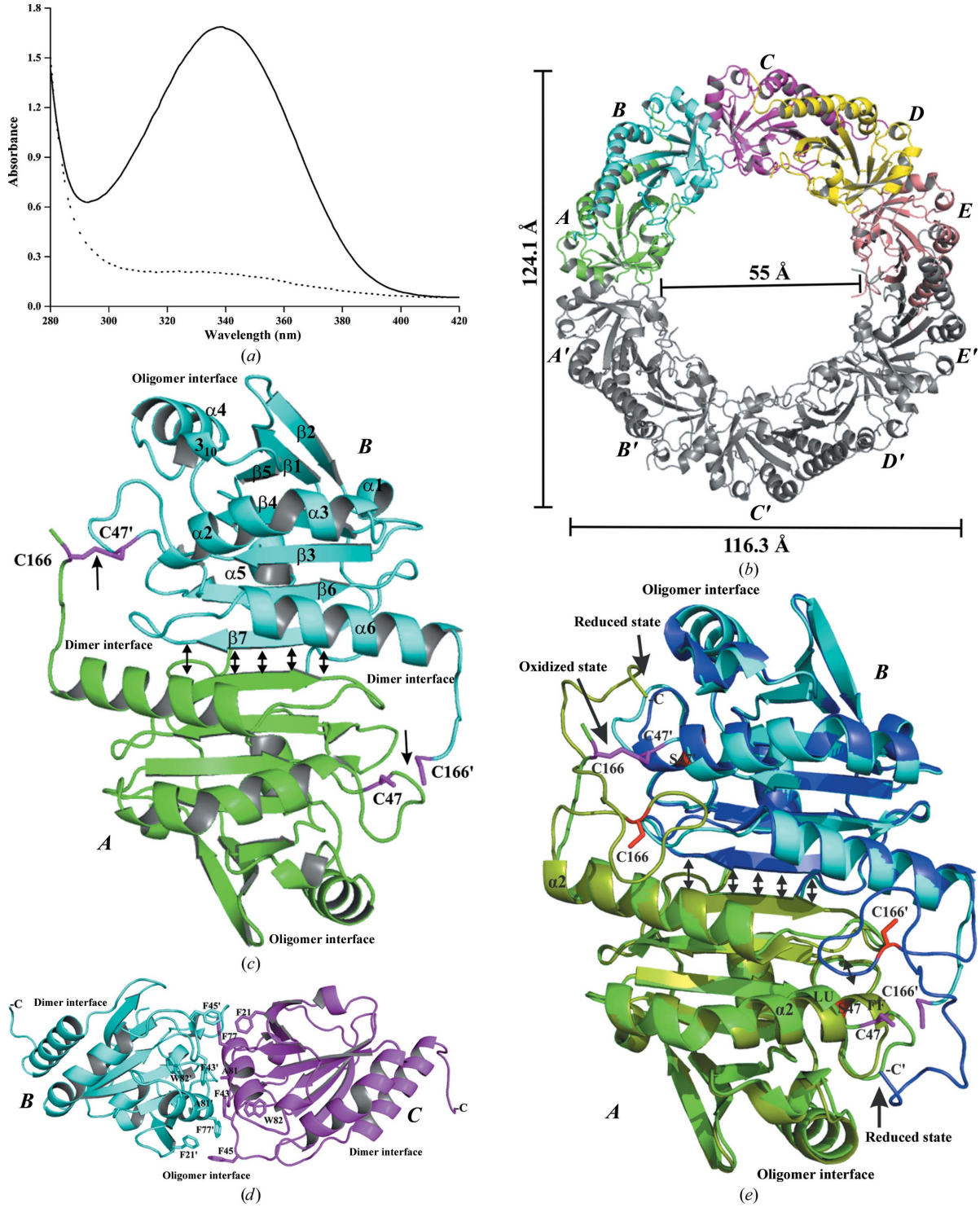

Figure 3
Structure and activity of *Ec*AhpC. (*a*) Measurement of the NADH-dependent peroxidase activity after addition of NADH (straight line), followed by measurement after 6 min (dotted line), demonstrates that NADH is oxidized by the catalytically active *Ec*AhpC–*Ec*AhpF complex. (*b*) The crystal structure of oxidized *Ec*AhpC in the decameric form $(\alpha_2)_5$, with an outer diameter of 124 × 116 Å and an inner diameter of 55 Å. Each asymmetric unit consists of five molecules (*A*–*E*), which are depicted in different colours; the crystallographic symmetry molecules are depicted in grey (*A*′–*E*′). (*c*) The dimer interface of *Ec*AhpC is shown between molecules *A* (green) and *B* (cyan). The redox-active cysteines (Cys47/Cys166′ and Cys47′/Cys166) are presented in magenta. Cys47′/Cys166 form an intermolecular disulfide bond and Cys47/Cys166′ are in the dithiol state. The interaction between the antiparallel β-strands of the two molecules at the dimer interface generates a continuous 14-stranded β-sheet in the dimer. (*d*) The oligomeric interface formed between chains *B* (cyan) and *C* (magenta) is predominantly stabilized by hydrophobic interactions. (*e*) Superposition of the oxidized *Ec*AhpC dimer *A* and *B* (green and cyan) and the reduced *St*AhC dimer *A* and *B* (olive green and blue; PDB entry 1n8j) indicates that the dimer interface at β and β' remains similar in both structures. The reduced *St*AhpC crystal structure revealed additional C-terminal residues. The C47S mutant and the Cys166 residues are coloured red and labelled. The peroxidative cysteine (Cys_P) present in the α_2 helix is in a fully folded (FF) conformation in the reduced state, while in the oxidized stated it is locally unfolded (LU) to facilitate disulfide formation.

plus *Ec*AhpC, respectively. A strong decrease in absorbance in the presence of *Ec*AhpC indicates high catalytic activity of the *Ec*AhpF–AhpC complex (Fig. 3*a*).

The crystal structure (3.3 Å resolution) of the enzymatically active *Ec*AhpC contains five molecules (chains *A*–*E*) in the asymmetric unit, forming a half-ring-shape conformation. The decameric ring complex consists of five homodimers $(\alpha_2)_5$ and its structure is generated by the crystallographic twofold symmetry operation (*A*′–*E*′; Fig. 3*b*). Each *Ec*AhpC monomer consists of a seven-stranded β-sheet located in the centre of the molecule, flanked on one side by four α-helices and on the other side by two α-helices (Figs. 3*c* and 3*d*). Each monomer contains two cysteine residues called the peroxidative cysteine (Cys_P47) and the resolving cysteine (Cys_R166). The monomer has two interfaces: a dimer interface and an oligomer interface. The dimer interface is mainly stabilized by salt-bridge and hydrogen-bond interactions between $\beta7$ and $\beta7'$ of each monomer, forming a combined 14-stranded β-sheet structure (Fig. 3*c*). The active site is composed of an intermolecular disulfide bond between Cys_P47 of one monomer and Cys_R166' of another monomer, interacting in a head-to-tail manner which contributes additional stabilization to the dimer interface (Fig. 3*c* and Supplementary Fig. S4*a*). The oligomeric assembly is mainly stabilized by hydrophobic interactions (Fig.3*d*).

The overall topology of oxidized *Ec*AhpC is similar to the *S. typhimurium* AhpC(C47S) mutant structure representing the so-called reduced state (PDB entry 1n8j; Wood *et al.*, 2003). A major difference between the oxidized *Ec*AhpC and the reduced *St*AhpC(C47S) structures involves the redox-active cysteines Cys_P47/Cys_R166 and the $\alpha2$ helix in which Cys_P47 is located (Figs. 3*c* and 3*e*). While Cys_P47 becomes exposed in the oxidized *Ec*AhpC owing to local unfolding of the $\alpha2$ helix, resulting in an intermolecular disulfide bond with Cys_R166' (Cys_P S—S Cys_R), the $\alpha2$ helix in the reduced state of the *St*AhpC(C47S) mutant structure winds into its fully folded conformation, moving Cys_P47 and Cys_R166' more than 10 Å apart and the sulfurs in opposite directions (Fig. 3*e*; Wood *et al.*, 2003). During hydroperoxide decomposition in *St*AhpC, Cys_P47 is oxidized to a cysteine sulfenic acid, which leads to local unfolding of the active site at Cys_P47, which converts the Cys_P loop to expose the resolving cysteine Cys_R166' with release of water to an intermolecular disulfide bond (Wood *et al.*, 2002).

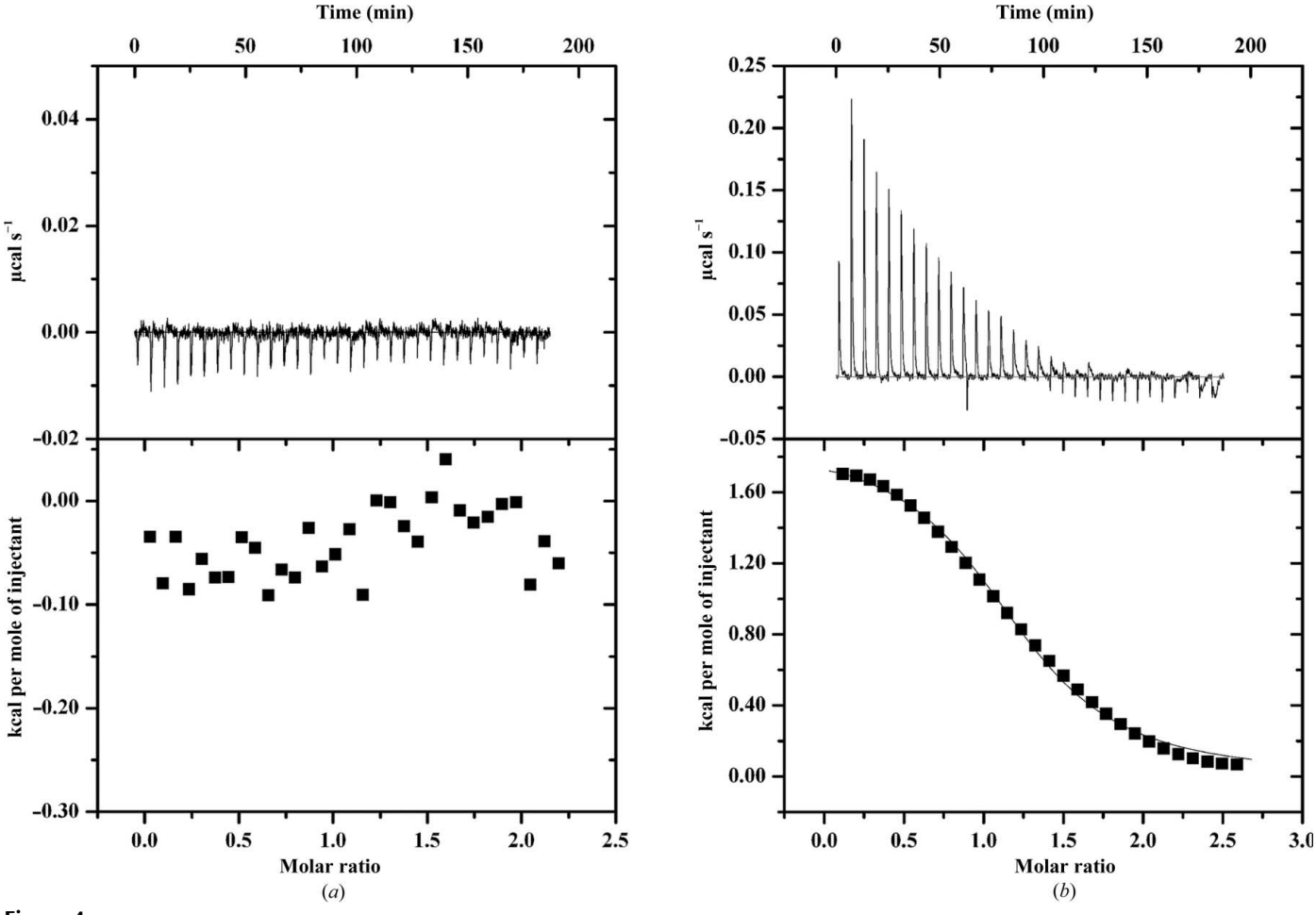

Figure 4
Binding-affinity measurements using isothermal titration calorimetry. Representative ITC profiles are shown for *Ec*AhpF-CTD (*a*) and *Ec*AhpF-NTD (*b*) with *Ec*AhpC. The top panel in the figures shows the injection profile after baseline correction and the bottom panel shows the integration (heat release) for each injection. The solid lines in the bottom panel reveal the fit of the data to a function based on a one-site binding model.

Table 3
Binding-affinity measurements for *Ec*AhpF-NTD and *Ec*AhpC using isothermal titration calorimetry.

The binding constants (K_a and K_d), enthalpy (ΔH), entropy ($T\Delta S$) and free-energy (ΔG) changes are provided.

	K_a ($\times 10^6\ M^{-1}$)	K_d (μM)	ΔH (kcal mol^{-1})	$T\Delta S$ (kcal mol^{-1})	ΔG (kcal mol^{-1})
NTD + AhpC	0.31 ± 0.09	3.2	2.86 ± 0.11	10.3	−7.50

3.4. *Ec*AhpC binds to the N-terminal domain of *Ec*AphF

Although the NTD of the bacterial AhpF has been proposed to bind to AhpC (Reynolds & Poole, 2000), to date no attempt had been made to characterize this interaction. Here, isothermal titration calorimetry (ITC) has been used to demonstrate that *Ec*AhpC interacts with the NTD of AhpF and to determine the binding constant of the interaction. Firstly, the recombinant *E. coli* proteins AhpF-NTD and AhpF-CTD were produced, including residues 1–196 of the N-terminal domain and residues 212–521 of the C-terminal domain of *Ec*AhpF, respectively (Supplementary Figs. S6*a* and S6*b*). Solution X-ray scattering data reveal that *Ec*AhpF-NTD forms a monomer and *Ec*AhpF-CTD is dimeric in solution (Supplementary Figs. S6*c* and S6*d*). As shown in the ITC experiments (Fig. 4), no interaction of *Ec*AhpF-CTD with *Ec*AhpC could be observed in the injection profile of *Ec*AhpF-CTD after baseline correction (top panel) and the profile of heat release per mole of injected subunits (bottom panel). In contrast, after titration of *Ec*AhpF-NTD with *Ec*AhpC an overall positive heat enthalpy could be detected, indicating an endothermic reaction (Fig. 4*b*). By using a single-site model equation, the binding isotherm could be fitted nicely and reflects equimolar binding of *Ec*AhpF-NTD to *Ec*AhpC. The dissociation constant (K_d) of about 3.2 μM indicates moderate binding between these two proteins (Table 3).

4. Discussion

4.1. An extended conformation of *E. coli* AhpF

The crystallographic structure of the elongated *Ec*AhpF presents for the first time an alternative conformation for the NTD, giving new insights into the electron-transfer mechanism with its substrate AhpC. To date, the crystallographic structure of the closed AhpF conformation from *S. typhimurium* (Wood *et al.*, 2001) and the C-terminal portion of *Ec*AhpF containing the FAD and NADH domains (Bieger & Essen, 2001) have been determined. The NTD of the present *Ec*AhpF adopts an extended open conformation with very well defined electron density. Apparently the NTD is flexible and is able to undergo conformational rearrangements (Wood *et al.*, 2001; Jönsson *et al.*, 2007). In the *Ec*AhpF crystal structure the NTD is involved in crystal-packing contact with a symmetry-related molecule. Solution X-ray scattering experiments and the scattering patterns computed from the crystallographic models of *Ec*AhpF and *St*AhpF (PDB entry 1hyu; Wood *et al.*, 2001) indicate that AhpF exists in solution as a dimer with an equal mixture of both extended open and closed conformations. This implies that the N-terminal domain oscillates between a closed and an open conformation in solution.

Structural comparisons between the full-length *Ec*AhpF (2.0 Å resolution) and *St*AhpF structures (Wood *et al.*, 2001) reveal that the folds of all four domains remain similar. The most significant structural difference observed is for the NTD, which adopts a compact conformation in *St*AhpF and adopts an elongated conformation in *Ec*AhpF (Fig. 5*a*). The NTD of *Ec*AhpF is rotated and translated by about 178° and 1.25 Å, respectively, when compared with that of *St*AhpF (compact conformation), and in *Ec*AhpF the NTD is stretched out, resulting in an elongated form (open conformation). The linker region residues from Lys201 to Glu205 are involved in the hinge motion for the NTD rotation, with the residues Lys201 and Arg202 likely to be important as they are highly disordered in the *Ec*AhpF structure. Because of the hinge motion, significant structural differences are observed in the linker region, reflected by the shorter helical region (Ala203–Asn208) in the open conformation of *Ec*AhpF compared with the longer helix (residues Lys201–Lys209) of *St*AhpF, which accommodates the large movement of the NTD in *Ec*AhpF. The bent conformation of the NTD in *St*AhpF makes extensive hydrogen-bond interactions with the FAD and NADH domains, which are missing in the NTD of the elongated *Ec*AhpF. In the open conformation the redox centre of the NTD is far away from the NADH redox centre (70 Å) whereas in the closed conformation it is at a distance of 33.2 Å.

The comparison between the structures also revealed a significant conformational difference in the NADH domain. The *St*AhpF NADH domain is rotated about 9° around and shifted about 0.79 Å along a screw axis running parallel to the centre of the molecule. The twisting region is formed by the residues Lys325–Arg327 and Gln448–Leu451, where Lys325, Trp326 and Gln448 act as a mechanical hinge. Although structurally similar, the redox centre of the NADH domain shows differences between the *Ec*AhpF and *St*AhpF structures. In *Ec*AhpF, the $_{345}$C*XX*C$_{348}$ motif sits above the flavin moiety of the FAD molecule, forming a short helix with a right-handed hook conformation, whereas in *St*AhpF the $_{345}$C*XX*C$_{348}$ motif adopts a nonhelical conformation and shifts away from the flavin moiety because of the bound chloride. There is no significant difference observed in the dimer interface between the two structures (Supplementary Fig. S5).

4.2. The structural requirements for an FO to a FR transition in *Ec*AhpF

The NTD and NADH domain of AhpF undergo conformational changes to transfer the reducing equivalent from NADH to the $_{345}$C*XX*C$_{348}$ motif in the NADH domain *via* flavin and subsequently to the $_{129}$C*XX*C$_{132}$ motif in the NTD, enabling AhpC reduction to occur (Poole *et al.*, 2000; Wood *et al.*, 2001). Because of the high structural similarity of *Ec*AhpF

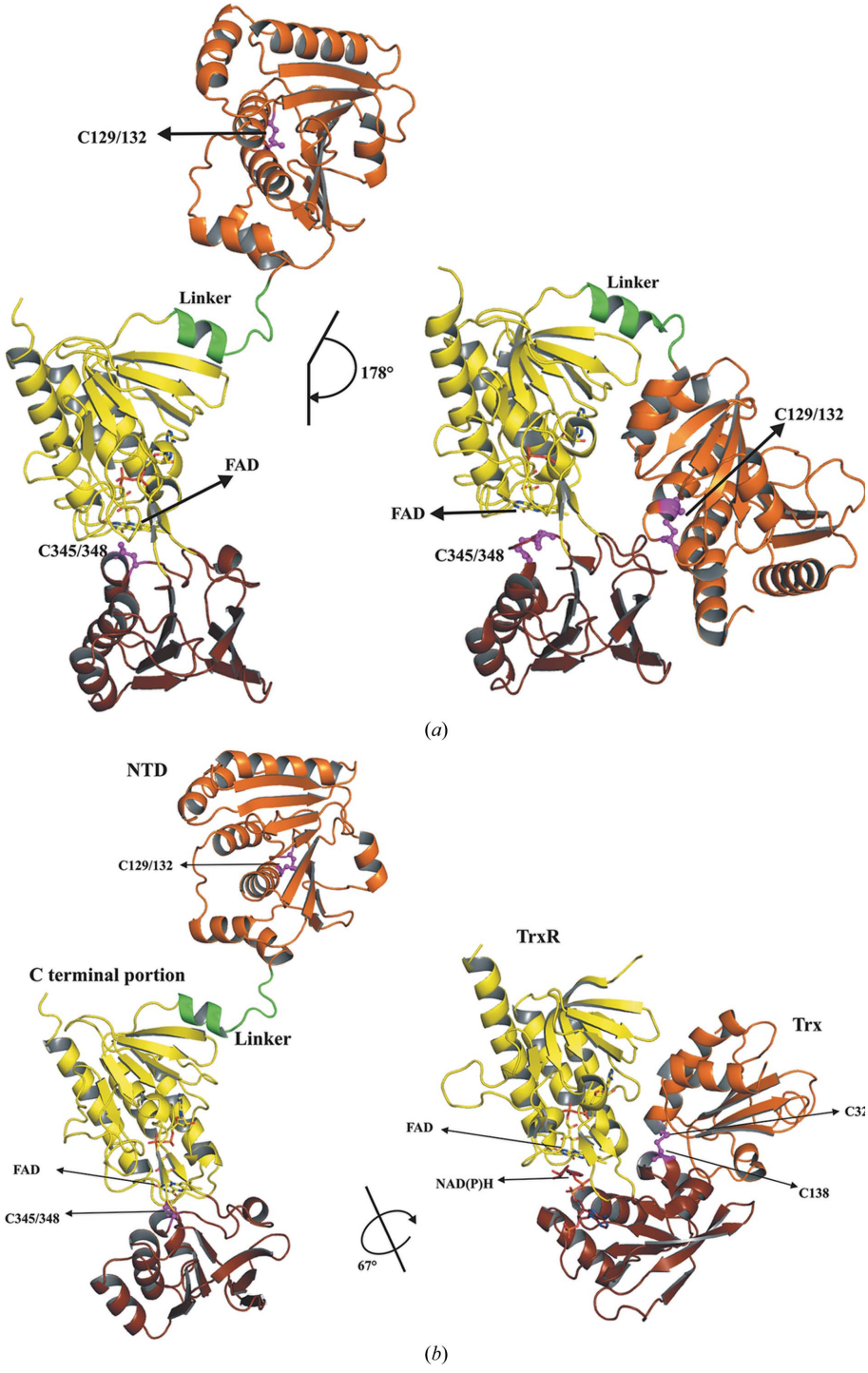

Figure 5
Structural comparison of *Ec*AhpF with *St*AhpF and *Ec*TrxR. (*a*) Comparison of individual domains of *Ec*AhpF with *St*AhpF yielded r.m.s. differences of 0.54, 0.64 and 0.72 Å for the backbone C^{α} atoms of the N-terminal, FAD and NADH domains, respectively. The most significant structural difference observed is the positioning of the NTD, which in *Ec*AhpF (left) is rotated and translated by about 178° and 1.25 Å compared with that in *St*AhpF (right). The helix in the linker region is locally unfolded (Ala203–Asn208) in *Ec*AhpF compared with *St*AhpF (Lys201–Lys209), allowing large domain movement to occur. (*b*) Comparison of the C-terminal segment of EcAhpF with EcTrxR (Langer *et al.*, 2013; PDB entry 1f6m). The superpositioning based on the FAD domain revealed that the NADH domain of TrxR undergoes a rotation of 67°. On assigning such a rotation to the NADH domain of the AhpF structures, the NTD of *St*AhpF (*a*, right) may need an additional conformational change between the redox centres of NTD (Cys129/Cys132) and the NADH domain (Cys345/Cys348) to enable the redox process to occur.

to the *E. coli* thioredoxin reductase (TrxR; Kuriyan *et al.*, 1991; Lennon *et al.*, 2000; Waksman *et al.*, 1994), the mechanism of *Ec*AhpF can be deduced to be analogous to that of *Ec*TrxR, as shown in Fig. 5(*b*). TrxR corresponds to the C-terminal portion and thioredoxin (Trx) to the NTD of AhpF. Two structural states of TrxR are known: the flavin-reducing (FR) state and the flavin-oxidized (FO) state (Kuriyan *et al.*, 1991; Lennon *et al.*, 2000; Waksman *et al.*, 1994). Structural comparison of the *Ec*AhpF C-terminal portion with TrxR from *E. coli* in the FO state (PDB entry 1trb) reveals an r.m.s.d. of 1.35 Å for 292 C^{α} positions, reflecting a high similarity (Kuriyan *et al.*, 1991; Waksman *et al.*, 1994). The FR conformation of *Ec*AhpF can be deduced by structural comparison to the FR state of *Ec*TrxR (Lennon *et al.*, 2000; Fig. 5*b*). When both structures are overlaid based on the FAD domain, a 67° rotation of the NADH domain of TrxR is revealed. When such a rotation is also applied to AhpF, the entire NADH domain comes closer to FAD, bringing the bound NADH to the *re* face of the isoalloxazine ring of flavin (Fig. 5*b*; Bieger & Essen, 2001; Lennon *et al.*, 2000; Wood *et al.*, 2001) and enabling electron transfer to occur. The rotation also brings the reduced dithiol (Cys345/Cys348) to the surface (Lennon *et al.*, 2000). In this exposed position it can easily be oxidized *via* the redox-active centre Cys129/Cys132 of the NTD. When the NADH domain turns 67° backwards, the $_{345}$C*XX*C$_{348}$ motif comes back to the *re* face of the isoalloxazine ring and the NAD^{+} to the surface for exchange with new NADH (Lennon *et al.*, 2000). During the rotation of the NADH domain, the NTD might not be in its compact conformation as shown in *St*AhpF (Wood *et al.*, 2001), otherwise severe clashes may occur between the NTD and the NADH domain (Figs. 5*a* and 5*b*). In addition, in the *St*AhpF structure the N-terminal domain bends towards the NADH domain and its $_{345}$C*XX*C$_{348}$ motif is exposed to the solvent and faces the other side from the redox centre (Fig. 5*a*). The distance between the disulfide centres is about 33 Å and does not depict the exact NTD

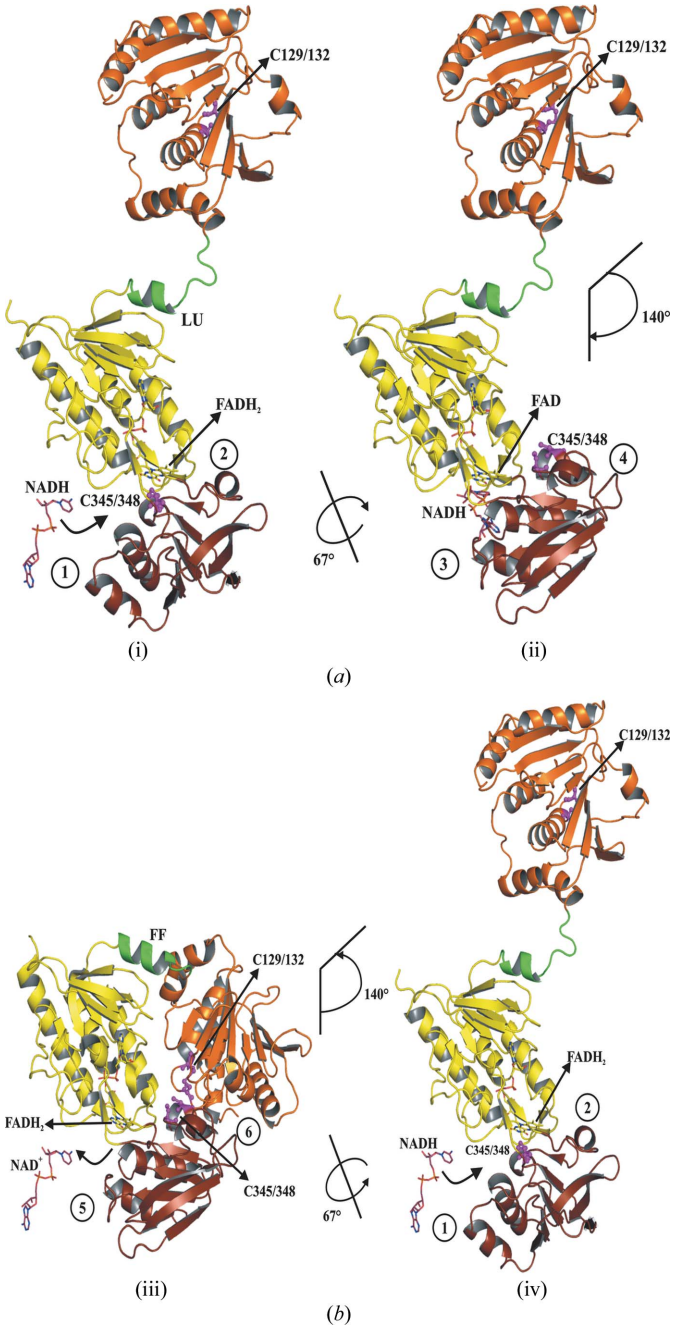

Figure 6
Proposed mechanism of the catalytic cycle of *Ec*AhpF. The *Ec*AhpF molecule is shown as a monomer for clarity. The catalytic process (i–iv) of AhpF includes two alternative conformations for the NTD and NADH domain. (*a*) (i) *Ec*AhpF in its open conformation: NADH binds to the NADH domain and $FADH_2$ reduces Cys345/Cys348. (ii) The NADH domain of *Ec*AhpF rotates by about 67°, bringing a bound NADH close to flavin and Cys345/Cys348 is exposed at the surface of the structure. In this conformation NADH is proposed to reduce FAD to $FADH_2$ and Cys345/Cys348 is in position to reduce Cys129/Cys132 of the NTD. (*b*) (iii) The NTD undergoes large conformational changes by rotating by around 140°, bringing Cys129/Cys132 closer to Cys345/Cys348 for hydride transfer. Subsequently, the NADH domain rotates back and releases NAD^+. The disulfide bond Cys345/Cyd348 also rotates back to a close distance to $FADH_2$, where it becomes reduced. (iv) The N-terminal domain rotates back into its open conformation to reduce the disulfide bond (Cys47/Cys166) of AhpC. The catalytic cycle of *Ec*AhpF restarts with the binding of NADH to the NADH domain.

reduction conformation. In this case, the NTD requires additional conformational changes of a rotation of about 100° and a shift by 8 Å in order to be reduced by the NADH domain (Jönsson *et al.*, 2007; Figs. 5*a* and 5*b*). Therefore, it can be proposed that the NTD remains, as in the *Ec*AhpF crystal structure, in an open and elongated conformation during NADH-domain rotation, where no steric hindrance occurs.

4.3. A proposed catalytic cycle for AhpF

The crystal and SAXS solution structures of *Ec*AhpF reveal the alternative conformations adopted by AhpF for catalysis, as shown in Fig. 6. Overall, it can be suggested that AhpF has two alternate movements: one of the NADH domain and another of the NTD. In *Ec*AhpF the NTD adopts a transiently open state to reduce AhpC and the NADH domain adopts the stable FO conformation, in which the NADH disulfide centre faces the flavin and does not interfere with AhpC reduction by the NTD. Once the dithiol–disulfide exchange with the AhpC catalytic centre is completed, the NTD redox centre replenishes itself by bending down towards the NADH-domain redox centre of the same monomer (Fig. 6; Supplementary Movie S1), in which the NADH domain twists into the FR state to donate electrons to the NTD and the substrate NADH moves close to the flavin. Both these conformational changes, the bending of the NTD and the twisting of the NADH domain, are likely to take place in a coordinated manner in order to trap the NTD by the NADH domain and to reduce the disulfide. From the open conformation of the *Ec*AhpF structure it might be concluded that the NTD does not necessarily need to bend by 178° as in the *St*AhpF structure but that a bend of about 140° would be sufficient to bring the NTD and NADH-domain redox centres into close proximity facing each other for reduction. Based on our proposed model (Fig. 6), the NTD does not necessarily interact with the FAD and NADH domains extensively as in *St*AhpF. The arrangement that we propose allows Cys348 of the NADH domain and Cys129 of the NTD to contact each other to initiate electron transfer to the NTD.

4.4. How the AhpC–AhpF ensemble provides an efficient redox process

Oxidized AhpC is only functionally active with peroxidative activity after reduction of its cysteines to their thiol form by AhpF. As shown in activity studies, AhpC is preferentially in a decameric form during catalysis (Chauhan & Mande, 2001; Kitano *et al.*, 1999; Nogoceke *et al.*, 1997) and is proposed to undergo a redox-sensitive dimer–decamer equilibrium (Wood *et al.*, 2002). Its functional partner *Ec*AhpF forms a dimer (Supplementary Fig. S1*a*) like the related TrxR (Lennon *et al.*, 2000). Considering the multimeric nature of both proteins, understanding of their complex formation is quite elusive. Our ITC data have revealed that *Ec*AhpC binds specifically *via* the NTD to *Ec*AhpF (Fig. 4*d*). Thus, a mechanistic model of AhpR can be proposed based on the structures presented here, in which the open conformation of the *Ec*AhpF homodimer allows electron transfer from two NTD redox-active

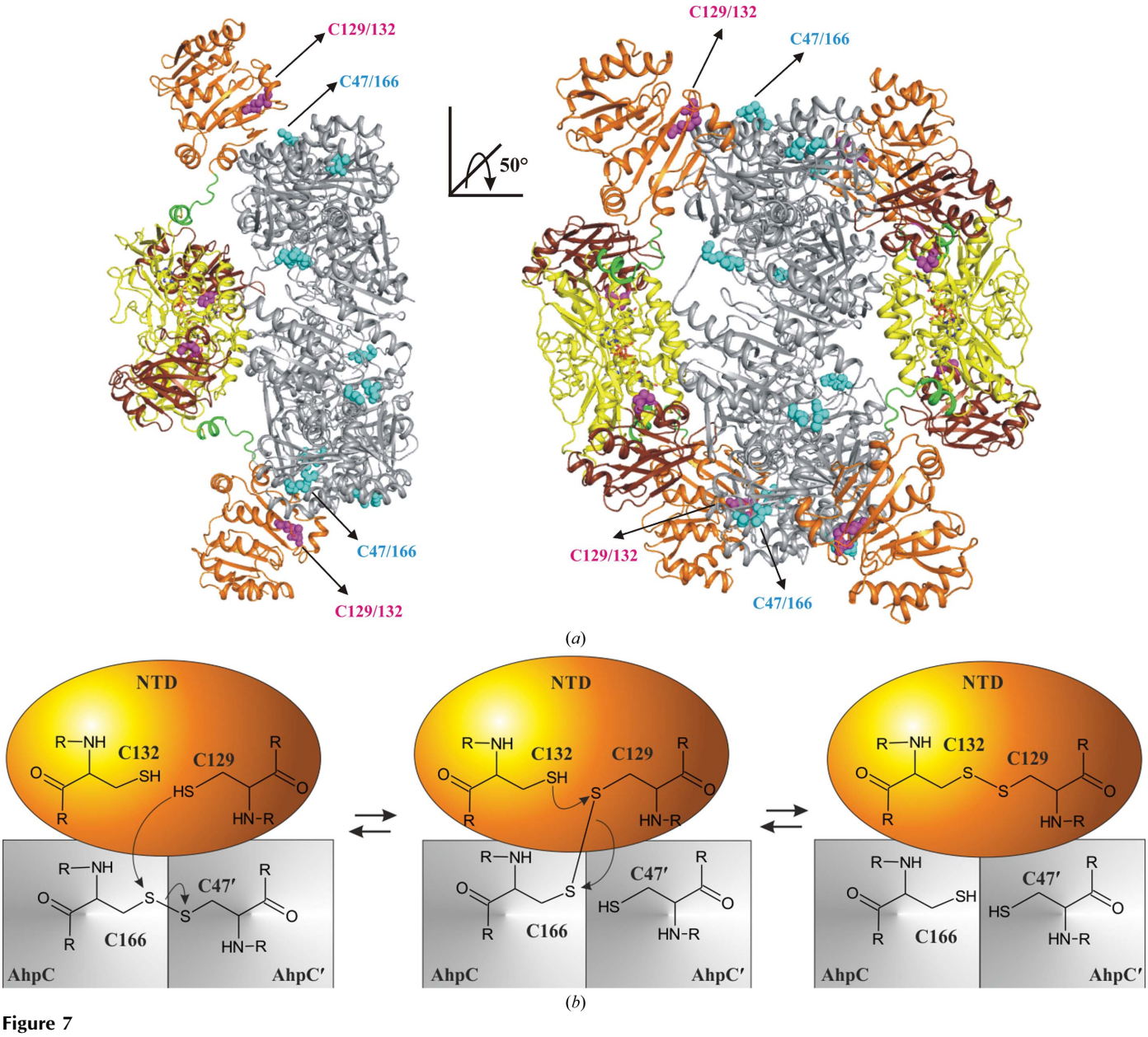

Figure 7
Ensemble formation of the alkylhydroperoxide reductase subunits AhpC and AhpF from *E. coli*. (*a*) The *Ec*AhpF homodimer is coloured according to its domains and the *Ec*AhpC decamer is shown in grey. The redox-active disulfide centres of the *Ec*AhpF and *Ec*AhpC molecules are shown as sphere representations in magenta and cyan, respectively. The distance between the two homodimer redox-active disulfide bonds Cys129/Cys132 of *Ec*AhpF is long enough to bridge the longest distance of 120 Å between two opposing redox-active disulfide bonds in the AhpC structure. We propose that two homodimeric AhpF molecules can be accommodated on the decameric AhpC. The right panel reveals the two *Ec*AhpF molecules facing each other on each side of the *Ec*AhpC decamer. (*b*) Proposed electron transfer between the redox-active centres of *Ec*AhpF and *Ec*AhpC. The final electron transfer of *Ec*AhpF is completed after hydride transfer from the crucial Cys129 to the partially exposed Cys166 of *Ec*AhpC.

disulfide bonds (Cys129/Cys132) to two redox-active disulfide bonds of *Ec*AhpC (Cys47/Cys166) (Fig. 7). Manual docking of the *Ec*AhpF homodimer to the *Ec*AhpC homodecamer shows that AhpF fits well to the AhpC ring (Fig. 7; Supplementary Movie S2). The side view reveals that both of the redox-active disulfides (Cys129/Cys132) in the NTD of *Ec*AhpF responsible for hydride transfer to (Cys47/Cys166) of AhpC are closely located. The advantage of ring formation of AhpC lies in the binding capacity for a second *Ec*AhpF homodimer, allowing the reduction of four redox-active disulfides (Cys129/Cys132) in *Ec*AhpC at the same time (Fig. 7; Supplementary Movie S2). Based on this model, Cys129 in the NTD of AhpF and the resolving cysteine (Cys_R166) of AhpC are exposed to each other, initiating the dithiol–disulfide exchange as shown in Fig. 7(*b*).

We thank the staff of beamline 13B1 at the National Synchrotron Radiation Research Centre (NSRRC), a national user facility supported by the National Science Council of Taiwan, ROC for expert help with data collection. The Synchrotron Radiation Protein Crystallography Facility at NSRRC is supported by the National Research Program for

Genomic Medicine. We acknowledge the staff of the S06 PX protein crystallography beamline at the Swiss Light Source (SLS) for expert help with data collection and for the provision of synchrotron radiation. This research was supported by the New Initiative Fund FY2010, NTU and financial support from the Nanyang Technological University to GG. PVD and WN are grateful to receive the SINGA scholarship (Singapore International Graduate Award).

References

Abrahams, J. P. & Leslie, A. G. W. (1996). *Acta Cryst.* D**52**, 30–42.
Adams, P. D., Mustyakimov, M., Afonine, P. V. & Langan, P. (2009). *Acta Cryst.* D**65**, 567–573.
Afonine, P. V., Grosse-Kunstleve, R. W., Echols, N., Headd, J. J., Moriarty, N. W., Mustyakimov, M., Terwilliger, T. C., Urzhumtsev, A., Zwart, P. H. & Adams, P. D. (2012). *Acta Cryst.* D**68**, 352–367.
Ames, B. N. (1983). *Science*, **221**, 1256–1264.
Amstad, P., Crawford, D., Muehlematter, D., Zbinden, I., Larsson, R. & Cerutti, P. (1990). *Bull. Cancer*, **77**, 501–502.
Battye, T. G. G., Kontogiannis, L., Johnson, O., Powell, H. R. & Leslie, A. G. W. (2011). *Acta Cryst.* D**67**, 271–281.
Bieger, B. & Essen, L.-O. (2001). *J. Mol. Biol.* **307**, 1–8.
Cerutti, P. A. (1985). *Science*, **227**, 375–381.
Chauhan, R. & Mande, S. C. (2001). *Biochem. J.* **354**, 209–215.
Chen, V. B., Arendall, W. B., Headd, J. J., Keedy, D. A., Immormino, R. M., Kapral, G. J., Murray, L. W., Richardson, J. S. & Richardson, D. C. (2010). *Acta Cryst.* D**66**, 12–21.
DeLano, W. (2002). *PyMOL*. http://www.pymol.org.
Emsley, P. & Cowtan, K. (2004). *Acta Cryst.* D**60**, 2126–2132.
Farr, S. B. & Kogoma, T. (1991). *Microbiol. Rev.* **55**, 561–585.
Floyd, R. A. (1990). *FASEB J.* **4**, 2587–2597.
Fridovich, I. (1978). *Science*, **201**, 875–880.
Grüber, G., Godovac-Zimmermann, J., Link, T. A., Coskun, Ü., Rizzo, V. F., Betz, C. & Bailer, S. M. (2002). *Biochem. Biophys. Res. Commun.* **298**, 383–391.
Guinier, A. & Fournet, G. (1955). *Small-angle Scattering of X-rays.* New York: Wiley.
Gutteridge, J. M. & Halliwell, B. (1989). *Baillieres Clin. Haematol.* **2**, 195–256.
Hayward, S. & Berendsen, H. J. C. (1998). *Proteins*, **30**, 144–154.
Hofmann, B., Hecht, H.-J. & Flohé, L. (2002). *Biol. Chem.* **383**, 347–364.
Jancarik, J. & Kim, S.-H. (1991). *J. Appl. Cryst.* **24**, 409–411.
Jönsson, T. J., Ellis, H. R. & Poole, L. B. (2007). *Biochemistry*, **46**, 5709–5721.
Kitano, K., Niimura, Y., Nishiyama, Y. & Miki, K. (1999). *J. Biochem.* **126**, 313–319.
Konarev, P. V., Volkov, V. V., Sokolova, A. V., Koch, M. H. J. & Svergun, D. I. (2003). *J. Appl. Cryst.* **36**, 1277–1282.
Kozin, M. B. & Svergun, D. I. (2001). *J. Appl. Cryst.* **34**, 33–41.
Krissinel, E. & Henrick, K. (2004). *Acta Cryst.* D**60**, 2256–2268.
Krissinel, E. & Henrick, K. (2005). *CompLife 2005*, edited by M. R. Berthold, R. Glen, K. Diederichs, O. Kohlbacher & I. Fischer, pp. 67–78. Berlin, Heidelberg: Springer.
Krissinel, E. & Henrick, K. (2007). *J. Mol. Biol.* **372**, 774–797.
Kuriyan, J., Krishna, T. S., Wong, L., Guenther, B., Pahler, A., Williams, C. H. & Model, P. (1991). *Nature (London)*, **352**, 172–174.
Laemmli, U. K. (1970). *Nature (London)*, **227**, 680–685.
Langer, G. G., Hazledine, S., Wiegels, T., Carolan, C. & Lamzin, V. S. (2013). *Acta Cryst.* D**69**, 635–641.
Lennon, B. W., Williams, C. H. Jr & Ludwig, M. L. (2000). *Science*, **289**, 1190–1194.
Link, A. J., Robison, K. & Church, G. M. (1997). *Electrophoresis*, **18**, 1259–1313.
McCoy, A. J., Grosse-Kunstleve, R. W., Adams, P. D., Winn, M. D., Storoni, L. C. & Read, R. J. (2007). *J. Appl. Cryst.* **40**, 658–674.
Murshudov, G. N., Skubák, P., Lebedev, A. A., Pannu, N. S., Steiner, R. A., Nicholls, R. A., Winn, M. D., Long, F. & Vagin, A. A. (2011). *Acta Cryst.* D**67**, 355–367.
Nelson, K. J., Parsonage, D., Hall, A., Karplus, P. A. & Poole, L. B. (2008). *Biochemistry*, **47**, 12860–12868.
Nogoceke, E., Gommel, D. U., Kiess, M., Kalisz, H. M. & Flohé, L. (1997). *Biol. Chem.* **378**, 827–836.
Otwinowski, Z. & Minor, W. (1997). *Methods Enzymol.* **276**, 307–326.
Poole, L. B. & Ellis, H. R. (1996). *Biochemistry*, **35**, 56–64.
Poole, L. B., Reynolds, C. M., Wood, Z. A., Karplus, P. A., Ellis, H. R. & Li Calzi, M. (2000). *Eur. J. Biochem.* **267**, 6126–6133.
Reynolds, C. M. & Poole, L. B. (2000). *Biochemistry*, **39**, 8859–8869.
Roberts, B. R., Wood, Z. A., Jönsson, T. J., Poole, L. B. & Karplus, P. A. (2005). *Protein Sci.* **14**, 2414–2420.
Seaver, L. C. & Imlay, J. A. (2001). *J. Bacteriol.* **183**, 7173–7181.
Sies, H. (1993). *Eur. J. Biochem.* **215**, 213–219.
Svergun, D. I. (1992). *J. Appl. Cryst.* **25**, 495–503.
Svergun, D. I. (1993). *J. Appl. Cryst.* **26**, 258–267.
Svergun, D., Barberato, C. & Koch, M. H. J. (1995). *J. Appl. Cryst.* **28**, 768–773.
Svergun, D. I., Petoukhov, M. V. & Koch, M. H. J. (2001). *Biophys. J.* **80**, 2946–2953.
Tartaglia, L. A., Storz, G., Brodsky, M. H., Lai, A. & Ames, B. N. (1990). *J. Biol. Chem.* **265**, 10535–10540.
Terwilliger, T. C. (2004). *Acta Cryst.* D**60**, 2144–2149.
Volkov, V. V. & Svergun, D. I. (2003). *J. Appl. Cryst.* **36**, 860–864.
Vonrhein, C., Blanc, E., Roversi, P. & Bricogne, G. (2007). *Methods Mol. Biol.* **364**, 215–230.
Vriend, G. (1990). *J. Mol. Graph.* **8**, 52–56.
Waksman, G., Krishna, T. S., Williams, C. H. Jr & Kuriyan, J. (1994). *J. Mol. Biol.* **236**, 800–816.
Winn, M. D. *et al.* (2011). *Acta Cryst.* D**67**, 235–242.
Winterbourn, C. C. & Hampton, M. B. (2008). *Free Radic. Biol. Med.* **45**, 549–561.
Wood, Z. A., Poole, L. B., Hantgan, R. R. & Karplus, P. A. (2002). *Biochemistry*, **41**, 5493–5504.
Wood, Z. A., Poole, L. B. & Karplus, P. A. (2001). *Biochemistry*, **40**, 3900–3911.
Wood, Z. A., Poole, L. B. & Karplus, P. A. (2003). *Science*, **300**, 650–653.